

Impact of Seismic Attenuation Corrections on Source Parameter Estimation

Dino Bindi 🔘 * 1, Matteo Picozzi 🜔 2, Adrien Oth 🕞 3, Daniele Spallarossa 🌔 4

Author contributions: Conceptualization: Dino Bindi, Matteo Picozzi, Adrien Oth, Daniele Spallarossa. Formal Analysis: Dino Bindi, Daniele Spallarossa. Writing - Original draft: Dino Bindi.

Abstract We estimate the stress drop $\Delta\sigma$ for 551 earthquakes from the 2019 Ridgecrest sequence in Southern California using a spectral decomposition. To assess the impact of propagation model assumptions, we apply a 2D cell-based approach that accounts for lateral attenuation variations and compare results with previous models using hypocentral distance (HYPO) and a set of attenuation models depending on source depth (EpiH). The 95% confidence interval for azimuthal-dependent 2D attenuation over an 80 km radius is 0.290 at 2 Hz and 0.473 at 14 Hz (log10 units). While the 2D model reveals significant azimuthal variations, the overall $\Delta\sigma$ distribution remains similar to that from the HYPO model, at least for the analyzed data set. High $\Delta\sigma$ is observed for the 2D model near the **M**7.1 and **M**6.4 events, while lower values appear at shallower depths, especially toward the Coso region and near the left-lateral fault junction of the **M**6.4 sequence. All three attenuation models consistently identify a high- $\Delta\sigma$ region at depths of 4–8 km between stations CLC (China Lake) and WRC2 (Renegade Canyon), located north of the M7.1 hypocenter where the main fault bends. Although spatial comparisons among models reveal some localized differences, the most significant impact arises when depth dependence is included in the attenuation model (EpiH), which effectively removes the increase of the average stress drop with depth.

Production Editor:
Andrea Llenos
Handling Editor:
Meng "Matt" Wei
Copy & Layout Editor:
Ethan Williams

Received: 17 March 2025 Accepted: 8 July 2025 Published: 21 August 2025

1 Introduction

The determination of source parameters is crucial for various applications, ranging from understanding rupture physics (e.g., Mori et al., 2003; Abercrombie and Rice, 2005) to defining input constraints for simulations (Molkenthin et al., 2014) and interpreting eventspecific ground motion variability in seismic hazard assessments (Baltay et al., 2013; Bindi et al., 2023c; Nie and Wang, 2025). However, estimating these parameters requires correcting for propagation and site effects. Focusing on spectral decomposition approaches (Andrews, 1986; Castro et al., 1990; Oth et al., 2011), a fundamental challenge lies in the non-uniqueness of the decomposition, necessitating constraints to mitigate trade-offs between source, propagation and site effects. Consequently, the retrieved source parameters inherently depend on the imposed assumptions. This issue has been highlighted in benchmarking efforts (Shible et al., 2022; Baltay et al., 2024), revealing both concerns and strengths. On the one hand, studies have demonstrated the significant impact of attenuation handling on source parameter estimates (Shearer et al., 2024). In particular, Abercrombie et al. (2021) demonstrated that the apparent depth dependence of stress drop is reduced when attenuation is modeled as a depth-dependent property. On the other hand, positive outcomes suggest consistency in certain aspects of the

methodologies (Mayeda et al., 2024). These findings underscore the importance of explicitly stating the applied constraints and thoroughly evaluating their influence.

To address this challenge, a logic tree approach has been proposed to assess the impact of model assumptions in relation to statistical uncertainties (Bindi et al., 2023a,b). Building on this framework, this study further investigates the effects of attenuation corrections by introducing a two-dimensional cell-based approach (Grendas et al., 2022; Chen et al., 2024). This approach aims to refine our understanding of how attenuation modeling influences source parameter estimations and to enhance the reliability of spectral decomposition methods. We apply these methodologies to the 2019 Ridgecrest earthquake sequence, as analyzed by Bindi et al. (2021), and compare the resulting stress drop estimates with a previous study that used different attenuation corrections (Bindi et al., 2023a). Additionally, we quantify and discuss the impact of attenuation assumptions both on the overall stress drop distribution and at the individual event level, examining spatial patterns in event-specific stress drop estimates.

2 Data

We use the dataset analyzed by Bindi et al. (2023a) within the framework of the Ridgecrest stress drop benchmark (Baltay et al., 2024). It consists of 551 earthquakes, with magnitudes ranging from 2.5 to 7.1 (Advanced National Seismic System Comprehensive Earth-

¹GFZ Helmholtz Centre for Geosciences, Potsdam, Germany, ²Istituto Nazionale di Oceanografia e di Geofisica Sperimentale OGS, Trieste, Italy, ³European Center for Geodynamics and Seismology, Walferdange, Luxembourg, ⁴University of Genova DIPTERIS, Genova, Italy

^{*}Corresponding author: dino.bindi@gfz.de

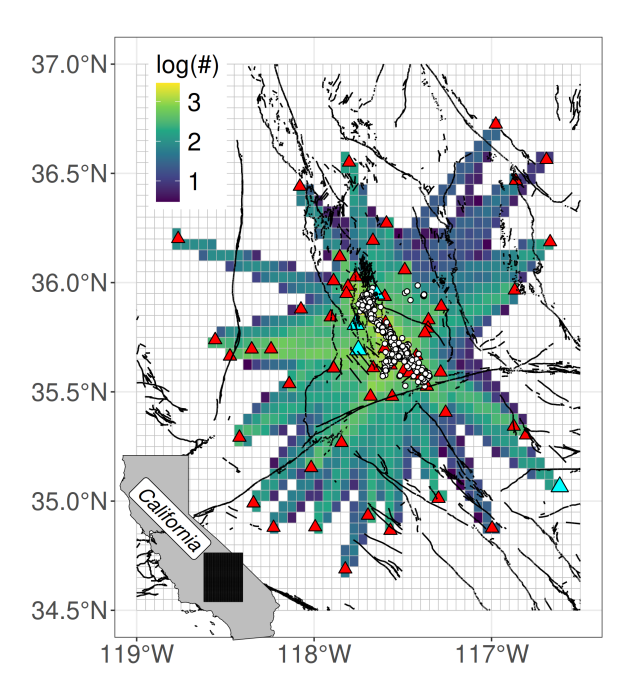


Figure 1 Location of analysed earthquakes (circles) and stations (triangles) in the Ridgecrest area (Southern California, black rectangle in the inset map). The site amplifications at the four stations filled in cyan are constrained to the results obtained by Bindi et al. (2023a). The grid cells used to determine the spectral attenuation are colored according to the logarithm of the number of source-station straight lines intersecting each cell. The traces of the fault systems (black lines) are taken from Evans et al. (2020).

quake Catalog, ComCat), recorded by 59 stations, considering both broadband sensors and accelerometers. The hypocentral depth distribution has a median of 4.6 km, with 10 and 90 percentiles equal to 1.78 km and 9.1 km, respectively. Among the various data processing techniques applied by Bindi et al. (2023a), we focus on the Fourier amplitude spectra in the frequency range 0.3-30 Hz, computed using 20-second time windows that encompass the main S-wave arrivals. For our analysis, we consider the horizontal components combined as the square root of the sum of the squared individual components. The spatial distribution of events and stations is shown in Figure 1, where the 0.05° by 0.05° grid used for the cell-based approach is also displayed. Additionally, the figure illustrates the number of source-tostation horizontal straight-lines crossing each cell.

3 Method

Following Bindi et al. (2023a), we apply a non-parametric spectral decomposition approach to isolate the source spectra from propagation and site amplification effects. This method, referred to as the Generalized Inversion Technique (GIT), leverages the redundancy in the dataset, where multiple stations record the same earthquake, and each earthquake is recorded at various

stations across different distances and azimuths. Considering $i=1,\ldots,N$ events recorded by $j=1,\ldots,M$ stations, GIT models the observed Fourier amplitude spectrum (FAS) at each frequency f as a convolution of the source spectrum $S_i(f)$, the propagation term $P_{ij}(f)$, and the site amplification $Z_j(f)$:

$$\log FAS_{ij}(f) = \log S_i(f) + \log P_{ij}(f) + \log Z_j(f). \quad (1)$$

The propagation term $P_{ij}(f)$ in equation 1 depends on the hypocentral distance R_{ij} or travel time T_{ij} between events i and station j. By considering all available eventstation combinations, equation 1 forms an overdetermined (for large datasets) linear system, which we solve using a least-squares approach (Koenker and Ng, 2021).

However, due to trade-offs among the terms in Equation 1, a priori constraints are necessary to remove unresolved degrees of freedom. Bindi et al. (2023a) constrained the average site amplification for a set of six selected stations to match the crustal amplification model of Campbell and Boore (2016) for the National Earthquake Hazards Reduction Program (NEHRP) B/C boundary, adjusted by a near-surface attenuation term controlled by $k_0 = 0.016$ s. The selected stations have measured V_{S30} (average shear-wave velocity of the uppermost 30 m) above 700 m/s (Rekoske et al., 2020) and do not show significant peaks of amplification. In this study, to mitigate trade-offs between source and site terms, we impose the site amplifications at stations TOW2, SRT, WCR2, and AVM (Figure 1) to match those determined by Bindi et al. (2023a). We analyze the solutions of Equation 1 using three different parameterizations of $P_{ij}(f)$. Specifically, in addition to the two models proposed by Bindi et al. (2023a):

- HYPO model: $P_{ij}(f)$ is parameterized as a function of discretized hypocentral distance intervals, assuming a uniform model for all depths;
- EpiH model: This model accounts for depthdependent variations by defining separate propagation models for different source depth ranges, with the attenuation models for each depth range simultaneously derived within a single inversion;

we introduce a third model based on a cell-based approach (Grendas et al., 2022; Lavrentiadis et al., 2023; Chen et al., 2024):

• 2D model: This approach incorporates a parametric representation of geometrical spreading while describing residual attenuation as a line integral over the entire ray path:

$$\log P_{ij} = -n \, \log R_{ij} + \sum_{k} \alpha_k \, d_{ijk}, \qquad (2)$$

where n is the unknown frequency-dependent geometrical spreading exponent; $k=1,\cdots,G$ indexes the cells in the two-dimensional grid; d_{ijk} is the length of the straight-line segment connecting event i to station j within cell k; α_k represents the unknown absorption coefficients within each cell. When solving Equation 1 using the parameterization in Equation 2, we impose the

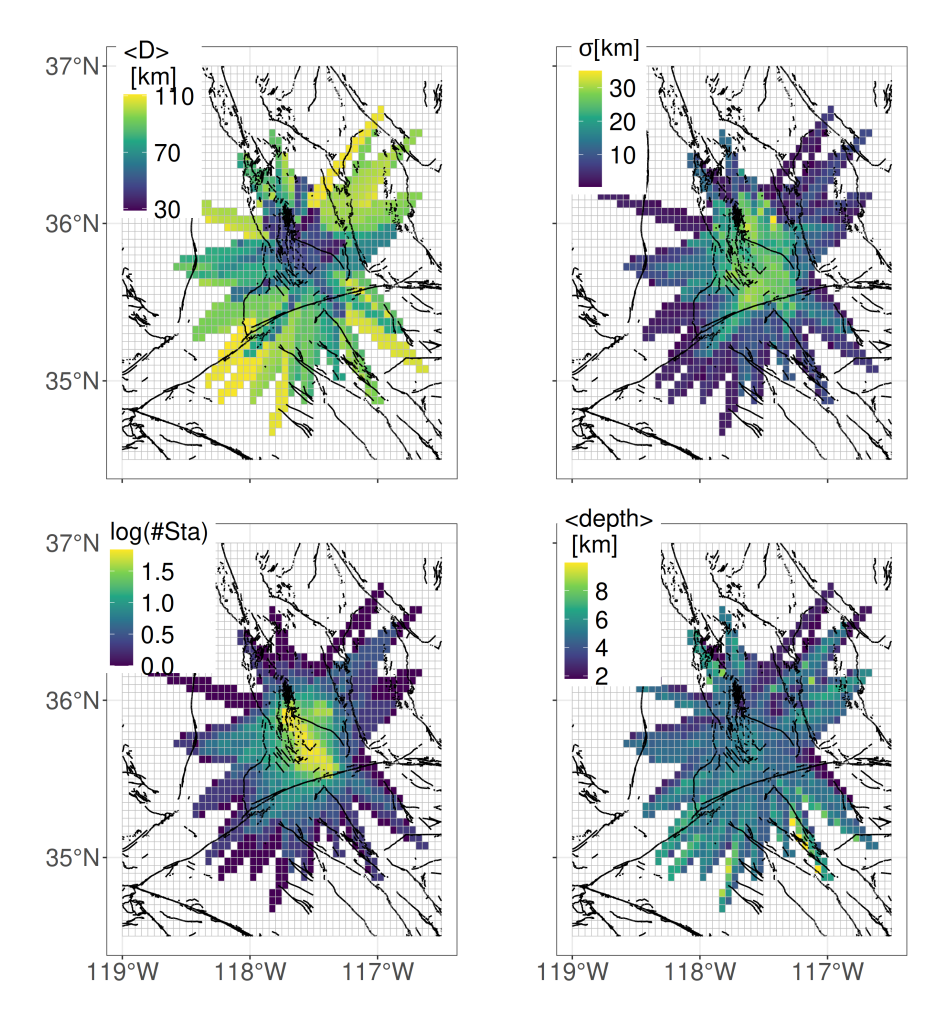


Figure 2 Different information about the intersection of the source-station rays and the cell-grid. a) the color scale represents the average hypocentral distance of the rays intersecting each cell; b) the color scale represents the standard deviation of the hypocentral distance of the rays intersecting each cell; c) the color scale represents the logarithm of the number of stations associated with the rays intersecting each cell; d) the color scale represents the average hypocentral depth of the rays intersecting each cell.

constraints that the absorption coefficients α_k are nonpositive and n>0.5, using the sparse quadratic programming solver developed by Stellato et al. (2020). Additionally, the sum of all d_{ijk} across the cells is scaled to match the total hypocentral distance R_{ij} , ensuring consistency with the overall attenuation framework. Results for α_k are only shown for cells k with at least 3 crossing rays.

4 Results on attenuation

Figure 2 shows some characteristics of the sampling of each cell. By construction, the 3D ray path from source to station is simplified by considering a 2D straight line connecting the epicentre to the receiving stations. Since both the information about the depth at which the ray crosses the volume below each cell and the length of the ray within the block below the cell (length that varies along the ray path and with the angle of incidence) are not accounted for by the planar geometry, the heterogeneity in the ray path coverage at depth could affect the ability to interpret the spatial distribution of the alpha coefficients in terms of lateral Q variability. Figures 2a and 2b show the mean and standard

deviation of the length of the rays crossing each cell. The area between 35.75 and 36 degrees latitude and -118 and -117.5 degrees longitude is characterised by relatively short ray paths with median hypocentral distance 45 km (and interquartiles equal to 43 km and 56 km, respectively), which therefore mostly sample the uppermost crustal layers; on the contrary, moving towards the boundary of the regions, cells tend to be sampled by longer ray paths, which propagate more deeply.

Furthermore, while the ray coverage for the inner part of the sample area is characterised by a large variety of event and station combinations (Figure 2c), the outer cells are mostly associated with one or few stations. Therefore, in the inner part of the study area, we achieve strong data redundancy and good azimuthal coverage. However, in the outer cells, the trade-off between propagation and site effects may be more pronounced, particularly in regions near station locations where 3D seismic rays emerge at the surface. Lastly, as shown in Figure 2d, there is a slight tendency for the southern portion of the study area to be sampled by rays originating, on average, from deeper events compared to the northern region.

The left panels of Figure 3 show the spatial distribu-

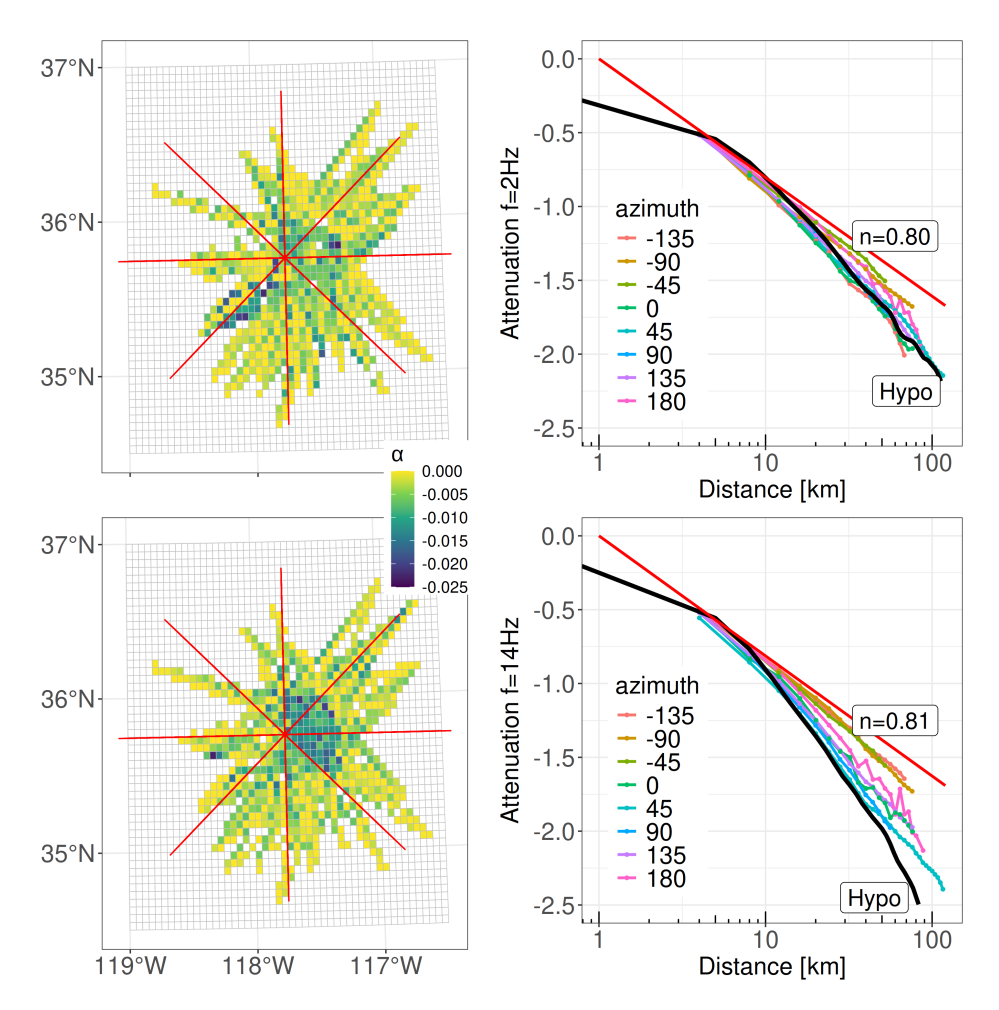


Figure 3 Attenuation results obtained for 2 Hz (top) and 14 Hz (bottom). The maps on the left show the spatial distribution of the absorption coefficients α_k in equation 2; the plots on the right show the attenuation with distance for eight different azimuths as shown corresponding to the red lines in the maps (the azimuths are measured with respect to North). The straight red line in the right-hand plots represents the geometrical spreading attenuation (the geometrical spreading coefficient n from equation 2 is given as a label); the black line labelled Hypo is the attenuation obtained by Bindi et al. (2023a) considering only the hypocentral distance, after applying an arbitrary vertical offset.

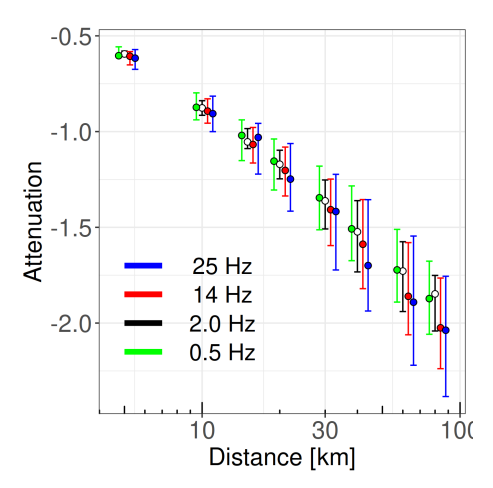


Figure 4 Median (circle) and 95% confidence interval (vertical error bar) of the attenuation coefficients α_k in equation 2 computed over circles of different radius (i.e., 5, 10, 15, 20, 30, 40, 60, and 80 km) centered in [-117.75,35.75] and azimuths every 5 degrees, considering the results for four different frequencies.

tion of the absorption coefficients α at 2 Hz and 14 Hz, while the right panels show the total attenuation (i.e., geometrical spreading and absorption along the path) with distance for 8 different azimuths corresponding to the red lines shown in the left panels. The attenuation with distance is compared with the HYPO model, whose attenuation curves (black curves) are arbitrarily shifted to match the 2D curves at about 4 km. The attenuation with distance associated with the geometrical spreading alone is also shown (red lines). Although the geometrical spreading exponent n is allowed to vary freely with frequency, its variability remains limited, ranging from 0.794 to 0.814, with values of 0.804 at 2 Hz and 0.813 at 14 Hz. The maps in Figure 3 reveal a clear spatial variability in the absorption coefficients, with distinct patterns emerging at higher frequencies. The azimuthal spread of the attenuation curves highlights an increasing spatial heterogeneity with frequency, showing stronger attenuation from the crossing point of the red lines in the left maps towards the east and northeast sectors, compared to the west. Additionally, at higher frequencies, the HYPO model exhibits a more rapid attenuation with distance.

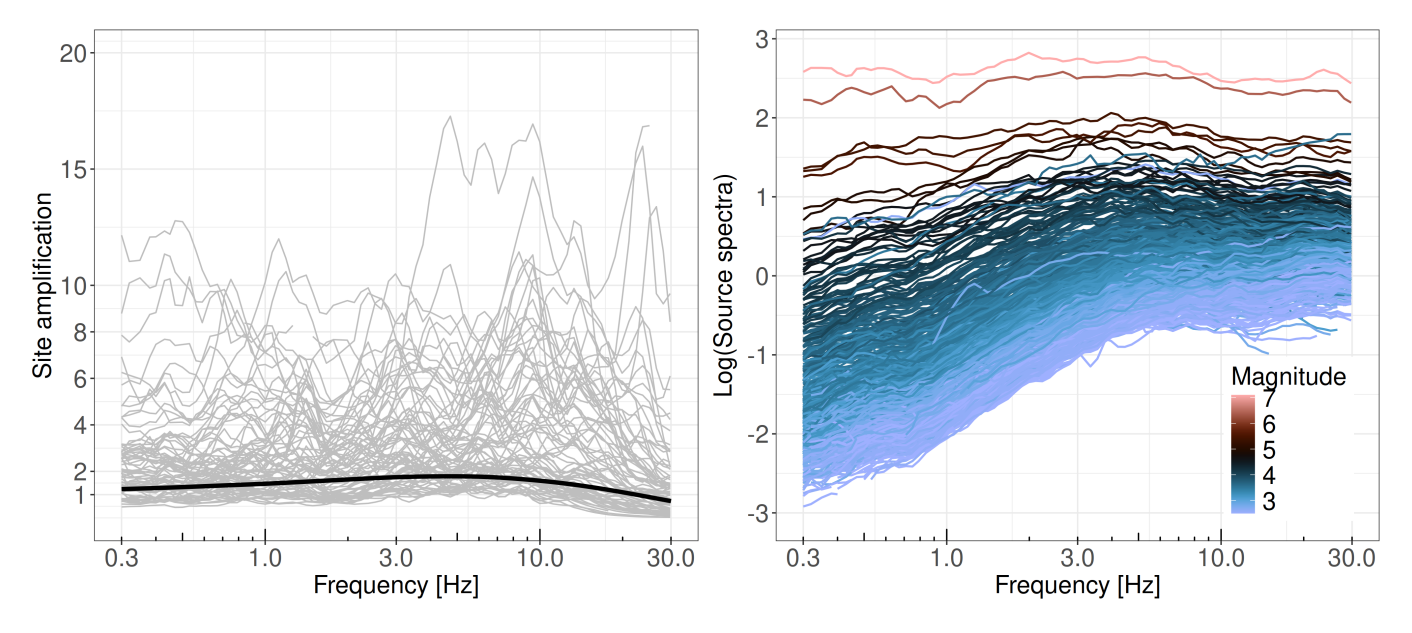


Figure 5 Site amplifications (left) and acceleration source spectra (right) obtained by the spectral decomposition after the correction for attenuation effects. In the left plot, the black curve represents the site amplification constraint applied to the reference stations; in the right plot, the source spectra are colored according to their magnitude.

To quantify the variability captured by the 2D model, Figure 4 shows the mean and standard deviation of the attenuation calculated over circles of increasing radii and centred as in Figure 3, considering the values for 0.5, 2, 14 and 25 Hz. In addition to showing the attenuation of the mean values with distance, Figure 4 also quantifies the variability captured by the 2D compared to the single-value attenuation for the homogeneous HYPO model. At 30 km, the 95% confidence interval for the log10 of the attenuation are 0.256 at 2 Hz and 0.347 at 14 Hz. This variability increases with distance, reaching 0.290 and 0.473, respectively, at 80 km. The observed increase in the confidence interval with frequency is consistent with expectations, reflecting the grater spatial heterogeneity of the absorption coefficients α at shorter wavelengths.

5 Results on source

The FAS corrected for the 2D attenuation model are inverted to separate the source and site terms. Figure 5 shows the distribution of the site amplifications (left) and acceleration source spectra (right). The obtained non-parametric source spectra are then fitted to the Brune omega-square source model (Brune, 1970) to estimate the seismic moment M_o and the corner frequency f_c :

$$S(f) = K(2\pi f)^2 \frac{M_o}{[1 + (\frac{f}{f_c})^2]},\tag{3}$$

where the constant K has been set so that the seismic moment of events with magnitudes between 3 and 5 matches on average the Advanced National Seismic System Comprehensive Earthquake Catalog (ComCat) moment magnitude (i.e., K is used to remove the average bias with respect to the ComCat catalog). The source parameters of the M6.4 and M7.1 events are not evaluated in this study. The stress drop is computed from M_o

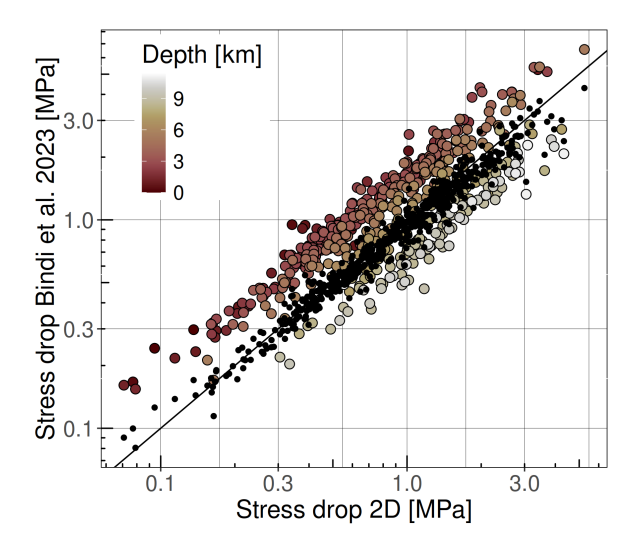


Figure 6 Comparison of the stress drop values obtained using different attenuation models. The results obtained in this study with the 2D attenuation model are shown along the x-axis; the results obtained by (Bindi et al., 2023a) using the HYPO (black circles) and the EpiH (circles colored according to the depth of the earthquake) attenuation models are reported along the y-axis.

and f_c by assuming a circular rupture of radius r with uniform stress drop (Eshelby, 1957; Keilis-Borok, 1959; Brune, 1970):

$$r = \frac{0.37\beta}{f_c},\tag{4}$$

$$\Delta \sigma = \frac{7}{16} \frac{M_o}{r^3}.$$
 (5)

In equation 4 we use the 3D velocity model by White et al. (2021) to estimate the shear wave velocity β at the hypocenter location.

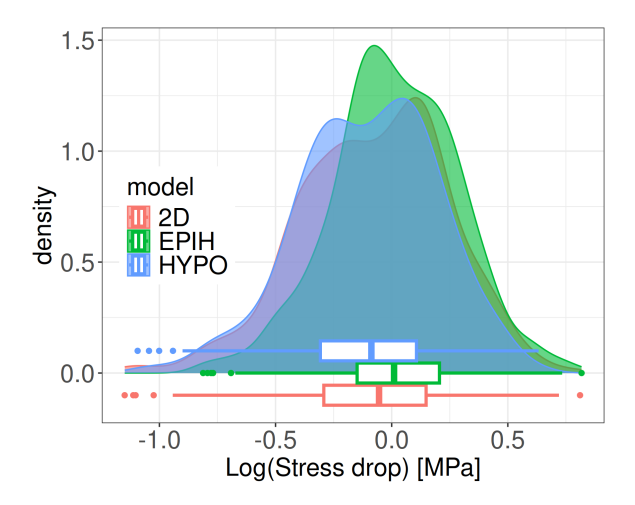


Figure 7 Comparison of the stress drop distributions computed considering the results shown in Figure 6. The different colors indicate different attenuation models, i.e., the 2D model of equation (1) and the HYPO and EpiH models by Bindi et al. (2023a).

Figure 6 compares the stress drop values obtained using the three attenuation models. The values from the 2D model are plotted along the x-axis, while those from the HYPO and EpiH models (Bindi et al., 2023a) are shown on the y-axis. On average, the results are consistent across models, though the EpiH model exhibits a larger spread that is influenced by depth. Although the overall stress drop distributions (Figure 7) are similar, with only slight differences in the median and interquartile range, the analysis of their differences reveals distinct patterns (Figure 8).

The 2D and HYPO models yield closely matching values, whereas the differences between the EpiH and 2D models display a larger spread and a positive mean shift of approximately 0.2 in log10 units, aligning with the trends observed in Figure 7. Furthermore, the histograms in Figures 8c and 8d confirm that these differences are depth-dependent, with hypocentral depth driving the observed variations. The color scale, which represents the average depth of events contributing to each bin, highlights this depth-controlled trend.

Figure 9 presents the stress drop values for individual earthquakes obtained using the 2D attenuation model, displayed in both map view and vertical projection. The pointwise distribution in the vertical projection is interpolated using kriging to generate a 2D stress drop map. Figure 10 compares the vertical stress drop sections derived from the three attenuation models, emphasizing differences in the amplitude of lateral and depth-dependent variations. To ensure the robustness of the results, only regions where the kriging variance falls below the 75th percentile of the overall cumulative variance distribution are displayed in Figure 10. Figure 11 complements this by showing the median stress drop as a function of depth for each attenuation model, as extracted from the corresponding sections in Figure 10.

6 Discussion

In the 2D cell-based approach, attenuation along the source-to-station ray path, after correcting for geometrical spreading, is distributed along a horizontal straight line based on the intersection length within each crossed cell. As a result, information from multiple ray paths propagating at different depths beneath each cell is mixed, making the depth at which the absorption coefficient is most representative dependent on the vertical sampling of rays passing below the cell. Given that this sampling can be highly heterogeneous across the study region, interpreting the 2D absorption map purely in terms of lateral variations in an apparent Q may not be fully justified. Coupling the source parameter estimation with a 3D Q tomography would allow to consider the impact of the 3D velocity and attenuation structure on the source parameters estimation (Scherbaum, 1990; Edwards et al., 2008; De Gori et al., 2023) but to perform a 3D frequency dependent Q tomography (Koulakov et al., 2010) is beyond the aim of the present study.

Although the dataset analyzed covers a limited area, and the used 2D approach considers only hypocentral distances between 15 and 100 km, Figure 2 indicates that the lateral contrasts observed in the absorption maps (Figure 3) can partially be attributed to the predominance of shorter ray paths in the central region, particularly in the eastern and northeastern sectors, sampling the uppermost layers. In contrast, longer ray paths, which dominate in the southern part of the study area and near its boundaries, are more representative of attenuation at greater depths. Despite this limitation, our primary objective is not to derive an attenuation map but to assess the impact of different approaches in capturing propagation effects. In this regard, the cell-based method provides a key advantage: it absorbs azimuthal variations in attenuation within the propagation term, preventing these variations from influencing the source term. Figures 3 and 4 illustrate a significant azimuthal variability in attenuation, which, as expected, is more pronounced at higher frequencies and larger distances. The variability of the 2D attenuation, quantified as extension of the 95% confidence interval of the azimuthal-dependent attenuation values measured over a circle of 80 km radius centered in (-117.5,35.75) is 0.290 at 2 Hz and 0.473 at 14 Hz, in log10 units. For a smaller radius of 30 km, the corresponding 95% confidence intervals are 0.256 and 0.347, respectively. This variability is not captured by the HYPO attenuation models, which parameterize attenuation solely as a function of hypocentral distance and frequency. From the perspective of non-ergodic ground motion models (Meng and Goulet, 2023), this represents a reduction in the path aleatory variability which is transferred to the epistemic uncertainty associated with the absorption coefficients, compared to a ground motion model that relies only on hypocentral distance as an explanatory variable.

The FASs corrected for the propagation are used to separate source and site contributions and the non parametric source spectra are in turn fitted to a Brune model

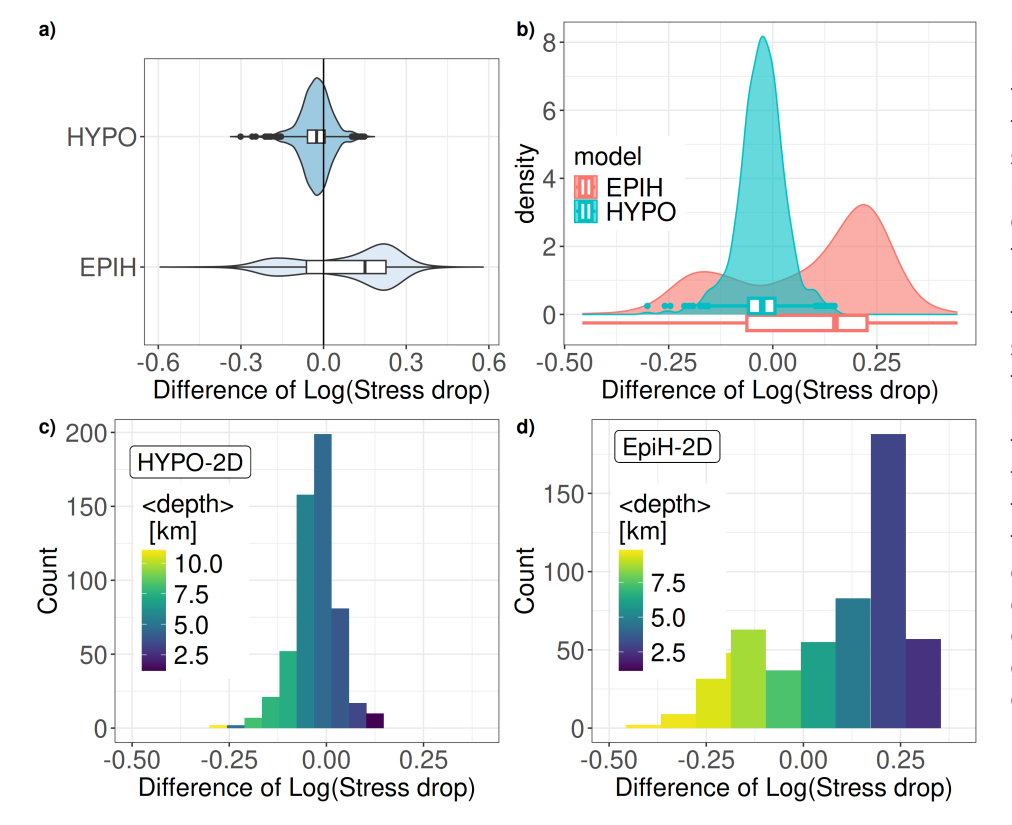
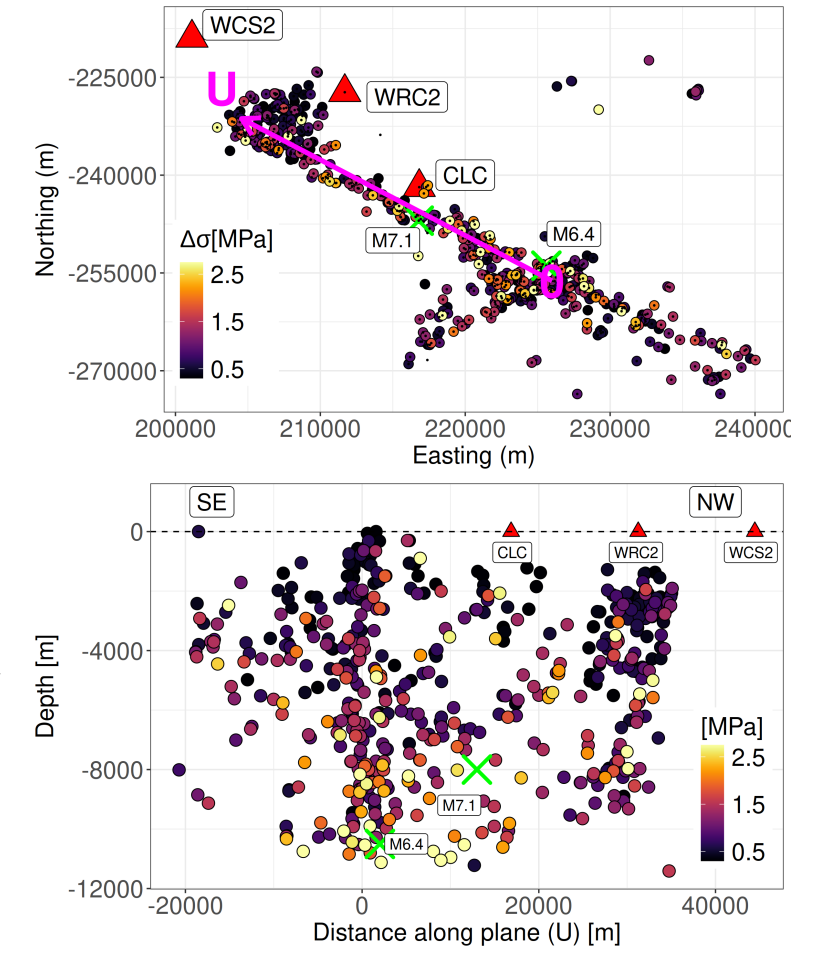


Figure 8 Distributions of the difference between the logarithm of the stress drops obtained in this study using the 2D attenuation model and the values computed considering the HYPO and EpiH attenuation models by Bindi et al. (2023a). a) violin plot representation of the distributions; b) the same as in panel a) but showing the density distributions and the box plots (median and interquartile range); c) histogram of the differences between the logarithm of the stress drops computed using the HYPO and 2D attenuation models. Each bin of the histogram is colored according to the average depth of the corresponding events. d) same as in panel c) but considering the difference between the EpiH and 2D results.

Figure 9 Top. Location of the analysed earthquakes in the NAD83, California Albers coordinate system, color coded with the stress drop of the events; the magenta arrow indicates the trace of the vertical plane used to construct the vertical section; the positive direction of the U-axis is towards North-West (NW), and 0 indicates its origin. Bottom. Orthogonal projections over the vertical plane intersecting the surface along the U-axis (upper frame); each circle is colored according to the stress drop value. Crosses indicate the hypocenters of the M6.4 and M7.1 earthquakes, not used for the stress drop analysis; triangles indicate the location of the CLC (China lake), WRC2 (Renegade canyon) and WCS2 (Coso Hot Springs 2) stations of the Southern California Seismic Network network (CI).



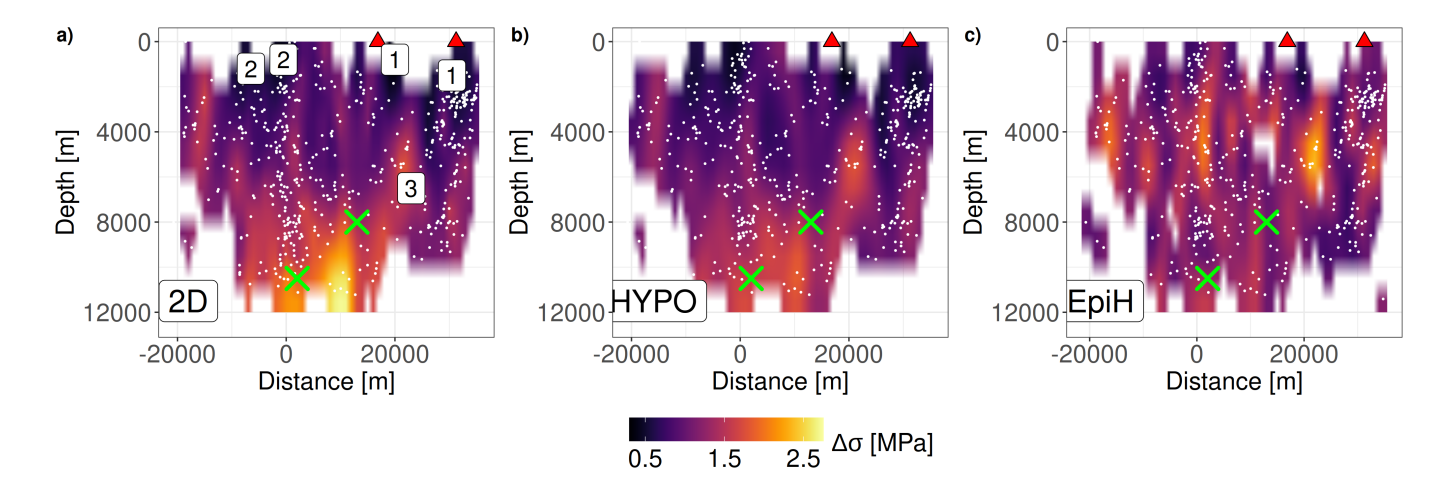


Figure 10 Kriging of the stress drop values over the vertical cross section of Figure 9 considering the 3 different attenuation models as indicated by the labels in each frame; small white dots indicate the projections of the event hypocenters; crosses indicate the hypocenters of the **M**6.4 and **M**7.1 events; triangles indicate the locations of the stations CLC and WRC2 of network CI (see Figure 9). Labels from 1 to 3 indicate areas discussed in the text.

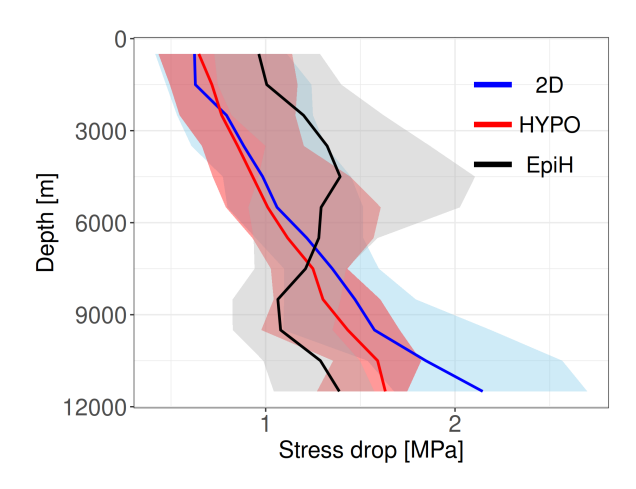


Figure 11 Median and 95% confidence interval of stress drop as function of depth, considering the results shown in Figure 10.

to determine seismic moment and corner frequency. When the stress drop distributions for the three attenuation models are considered, the overall statistical characteristics are similar. The mean and standard deviation of $\log \Delta \sigma$ for the HYPO, EPIH and 2D models are (-0.103 ± 0.30) , (0.015 ± 0.273) , and $(-0.05 \pm$ 0.301), respectively. The standard deviations we obtain agree with Chen et al. (2025), who found that, when applied to the Ridgecrest dataset, a spectral decomposition method with depth-dependent attenuation produced the smallest stress drop variability. When the distributions of the $\log \Delta \sigma$ differences are analysed, the HYPO and 2D models provide a zero-mean distribution with a small spread (the standard deviation of the differences is 0.06). On the contrary, the EpiH-2D differences show a large spread (the 2.5th and 97.5th percentiles are -0.249 and 0.324, respectively), with a positive median (0.15) and a bi-modal shape. The variability of the differences is controlled by depth and the two modes of the distribution correspond to average depths of about 8.7 km and 2.9 km.

Previous studies have shown that stress drop values in the study area exhibit significant variability over just a few kilometers (Trugman, 2020; Vandevert et al., 2024). This variability suggests that the Ridgecrest sequence activated a complex network of faults with different sizes and geometries (Ross et al., 2019; Shelly, 2020) within a heterogeneous stress environment. Therefore, to identify spatially coherent patterns common to the stress drop estimates from the three attenuation models, we apply a kriging interpolation to stress drop values projected onto a vertical plane, as illustrated in Figure 9. The 2D (Figure 10a) and HYPO (10b) attenuation models reveal stress drop patterns consistent with previous studies (e.g., Trugman, 2020) (and references therein). A high-stress-drop region is observed near the hypocenters of the mainshocks (marked by crosses), with the 2D model showing the largest amplitudes. Lower stress drop values are concentrated at shallower depths (Figures 10a,b), particularly towards the northwestern edge of the study region (label 1 in Figure 10a) near station WRC2 (Figure 9) and at the junction with the left-lateral orthogonal fault that ruptured during the M6.4 sequence (the low stress drop area is extending southward from distance zero, label 2 in Figure 10a). Additionally, a high-stress-drop zone (label 3) is detected at depths of approximately 4 to 8 km in the region between stations CLC and WRC2 (triangles in Figure 10), where the main fault associated with the M7.1 mainshock exhibits a bend (e.g., Goldberg et al., 2020).

While the interpolated stress drop maps from the HYPO and 2D models display similar spatial patterns, the 2D model generally produces higher stress drop amplitudes at depth. In contrast, the EpiH model (Figure 10c) amplifies the lateral stress drop contrasts at shallow depths while reducing or even inverting the vertical stress drop gradient (see also Figure 6). Therefore, the comparison in Figure 10 suggests that incorporating hypocentral depth into the attenuation model (i.e., using different attenuation models for different depth ranges as for EpiH) has a greater influence on the results than accounting for lateral variations through the

cell-based approach, in agreement with the conclusion drawn by Zhang et al. (2022) for the Parkfield borehole network. This observation is further supported by the median $\Delta \sigma$ profiles with depth shown in Figure 11, derived from the corresponding sections in Figure 10. The HYPO and 2D models yield very similar results, with noticeable differences only at the greatest depths (see also Figures10a,b). In contrast, the EPIH model produces less variable $\Delta \sigma$ values overall, with average values higher than 2D and HYPO above 8 km and lower values at greater depths. The EPIH results show a positive $\Delta \sigma$ gradient with depth above 5 km and below 9 km, while exhibiting a negative gradient in the intermediate depth range. Overall, the results in Figure 11 underscore the strong sensitivity of spatial variability of the source parameter estimates to the assumptions made about depth-dependent attenuation in the underlying models.

7 Conclusions

We estimated the stress drop of the 551 earthquakes from the 2019 Ridgecrest sequence using a spectral decomposition approach that incorporates a cell-based grid model for the attenuation term. While representing 3D wave propagation with a planar cell-based model limits the direct interpretation of the resulting absorption coefficients as a fully anelastic attenuation map, this simplified approach offers the advantage of allowing the propagation term in the spectral decomposition to partially account for lateral variations in attenuation. This, in turn, shifts part of the aleatory variability to epistemic uncertainty associated with the 2D attenuation model. When comparing the stress drop distributions obtained using three different approaches to capture spectral attenuation, we find that the overall distributions are consistent and scale approximately one-toone with each other. However, the model that explicitly accounts for depth-dependent attenuation exhibits a larger spread in stress drop values, with depth exerting a significant influence.

A spatial comparison of individual stress drop values, including cross-sectional maps obtained via kriging, reveals that the 2D cell-based approach produces spatial patterns similar to those observed in the hypocentral distance attenuation model, albeit with larger amplitudes at depth. The key features are also consistent with findings from previous studies. Specifically, we observe a pattern of high stress drop in the region where the M7.1 and M6.4 earthquakes occurred, while low stress drop values are concentrated at shallower depths, particularly at the northeastern boundary of the study area (toward the Coso region) and at the junction with the left-lateral fault activated during the **M**6.4 sequence. The stress drop map generated by the depth-dependent attenuation model enhances the contrast of shallow patterns while reducing or even inverting the depth gradient. Additionally, all three models consistently identify a region of high stress drop between 4 and 8 km depth in the area between stations CLC and WRC2, north of the **M**7.1 hypocenter, where the primary fault exhibits a bend.

In conclusion, introducing an attenuation model that accounts for lateral variations in attenuation does not significantly alter the overall stress drop distribution compared to a simple distance-dependent model. While spatial comparisons reveal more localized differences, the most pronounced impact arises when the attenuation model incorporates depth dependence.

Acknowledgements

We thank the two anonymous reviewers and the editor Meng Wei for their constructive comments and suggestions, which helped to improve the clarity and quality of the manuscript.

Data and code availability

This study has been performed within the framework of the community stress-drop validation study (Baltay et al., 2024). Waveforms and metadata can be found at https://www.scec.org/research/stress-drop-validation. Data from the following seismic networks have been analyzed: CI (California Institute of Technology and United States Geological Survey Pasadena, 1926), GS (Albuquerque Seismological Laboratory (ASL)/USGS, 1980), SN (University of Nevada, Reno, 1992), NN (University of Nevada, Reno, 1971), PB (Plate Boundary Observatory Borehole Seismic Network, UNAVCO, not registered), and ZY_1990 (Portable Southern California Seismic Networks, Caltech, not registered).

Analyses have been performed in R (R Core Team, 2024) using packages: ggplot2 (Wickham, 2016), dplyr (Wickham et al., 2022), sf (Pebesma, 2018), gstat (Gräler et al., 2016), sp (Pebesma and Bivand, 2005), osqp (Stellato et al., 2020), sparseM (Koenker and Ng, 2021), viridis (Garnier et al., 2021), cowplot (Wilke, 2020), rnaturalearth (Massicotte and South, 2023). The under development project for hosting the modules for spectral decomposition analysis is available at https://gitlab.rm.ingv.it/inversion/gitpy

Competing interests

The authors declare to have no competing interests.

References

Abercrombie, R. E. and Rice, J. R. Can observations of earthquake scaling constrain slip weakening? *Geophysical Journal International*, 162(2):406–424, 2005. doi: https://doi.org/10.1111/j.1365-246X.2005.02579.x.

Abercrombie, R. E., Trugman, D. T., Shearer, P. M., Chen, X., Zhang, J., Pennington, C. N., Hardebeck, J. L., Goebel, T. H. W., and Ruhl, C. J. Does Earthquake Stress Drop Increase With Depth in the Crust? *Journal of Geophysical Research:* Solid Earth, 126(10):e2021JB022314, 2021. doi: https://doi.org/10.1029/2021JB022314.

Albuquerque Seismological Laboratory (ASL)/USGS. US Geological Survey Networks [Data set], 1980.

- Andrews, D. J. Objective Determination of Source Parameters and Similarity of Earthquakes of Different Size, pages 259–267. American Geophysical Union (AGU), 1986. doi: https://doi.org/10.1029/GM037p0259.
- Baltay, A., Abercrombie, R., Chu, S., and Taira, T. The SCEC/USGS Community Stress Drop Validation Study Using the 2019 Ridgecrest Earthquake Sequence. *Seismica*, 3(1), 2024. doi: 10.26443/seismica.v3i1.1009.
- Baltay, A. S., Hanks, T. C., and Beroza, G. C. Stable Stress-Drop Measurements and their Variability: Implications for Ground-Motion Prediction. *Bulletin of the Seismological Society of America*, 103 (1):211–222, 02 2013. doi: 10.1785/0120120161.
- Bindi, D., Razafindrakoto, H. N. T., Picozzi, M., and Oth, A. Stress Drop Derived from Spectral Analysis Considering the Hypocentral Depth in the Attenuation Model: Application to the Ridgecrest Region, California. *Bulletin of the Seismological Society of America*, 111(6):3175–3188, 2021. doi: 10.1785/0120210039.
- Bindi, D., Spallarossa, D., Picozzi, M., Oth, A., Morasca, P., and Mayeda, K. The community stress-drop validation study—Part I: Source, propagation, and site decomposition of Fourier spectra. *Seismological Society of America*, 94(4):1980–1991, 2023a.
- Bindi, D., Spallarossa, D., Picozzi, M., Oth, A., Morasca, P., and Mayeda, K. The community stress-drop validation study—part II: Uncertainties of the source parameters and stress drop analysis. *Seismological Society of America*, 94(4):1992–2002, 2023b.
- Bindi, D., Zaccarelli, R., Cotton, F., Weatherill, G., and Reddy Kotha, S. Source Scaling and Ground-Motion Variability along the East Anatolian Fault. *The Seismic Record*, 3(4):311–321, 2023c. doi: 10.1785/0320230034.
- Brune, J. N. Tectonic stress and the spectra of seismic shear waves from earthquakes. *Journal of Geophysical Research (1896-1977)*, 75(26):4997–5009, 1970. doi: https://doi.org/10.1029/JB075i026p04997.
- California Institute of Technology and United States Geological Survey Pasadena. Southern California Seismic Network [Data set]. International Federation of Digital Seismograph Networks, 1926
- Campbell, K. W. and Boore, D. M. Evaluation of Six NEHRP B/C Crustal Amplification Models Proposed for Use in Western North America. *Bulletin of the Seismological Society of America*, 106(2): 673–686, 2016. doi: 10.1785/0120150242.
- Castro, R. R., Anderson, J. G., and Singh, S. K. Site response, attenuation and source spectra of S waves along the Guerrero, Mexico, subduction zone. *Bulletin of the Seismological Society of America*, 80(6A):1481–1503, 1990. doi: 10.1785/BSSA08006A1481.
- Chen, K., Chen, X., Wang, Y., and Li, X. Source Scaling, Spatially Variable Path Attenuation, and Site-Effect Parameters via a Generalized Inversion Technique for Strong-Motion Data from Sichuan, China. *Bulletin of the Seismological Society of America*, 114(5): 2504–2523, 05 2024. doi: 10.1785/0120230268.
- Chen, X., Wu, Q., and Pennington, C. Factors That Influence Variability in Stress-Drop Measurements Using Spectral Decomposition and Spectral-Ratio Methods for the 2019 Ridgecrest Earthquake Sequence. *Bulletin of the Seismological Society of America*, 2025. doi: 10.1785/0120240150.
- De Gori, P., Pio Lucente, F., and Chiarabba, C. Source-Parameter Estimation after Attenuation Correction through the Use of Q Tomography. *Bulletin of the Seismological Society of America*, 113 (4):1739–1758, 2023. doi: 10.1785/0120220196.
- Edwards, B., Rietbrock, A., Bommer, J. J., and Baptie, B. The Acquisition of Source, Path, and Site Effects from Microearthquake Recordings Using Q Tomography: Application to the United Kingdom. *Bulletin of the Seismological Society of America*, 98(4): 1915–1935, 08 2008. doi: 10.1785/0120070127.

- Eshelby, J. D. The determination of the elastic field of an ellipsoidal inclusion, and related problems. *Proceedings of the Royal Society of London. Series A. Mathematical and Physical Sciences*, 241 (1226):376–396, 1957. doi: 10.1098/rspa.1957.0133.
- Evans, W. S., Plesch, A., Shaw, J. H., Pillai, N. L., Yu, E., Meier, M., and Hauksson, E. A Statistical Method for Associating Earthquakes with Their Source Faults in Southern California. *Bulletin of the Seismological Society of America*, 110(1):213–225, 2020. doi: 10.1785/0120190115.
- Garnier, Simon, Ross, Noam, Rudis, Robert, Camargo, Pedro, A., Sciaini, Marco, Scherer, and Cédric. *viridis Colorblind-Friendly Color Maps for R*, 2021. R package version 0.6.2.
- Goldberg, D. E., Melgar, D., Sahakian, V. J., Thomas, A. M., Xu, X., Crowell, B. W., and Geng, J. Complex Rupture of an Immature Fault Zone: A Simultaneous Kinematic Model of the 2019 Ridgecrest, CA Earthquakes. *Geophysical Research Letters*, 47(3):e2019GL086382, 2020. doi: https://doi.org/10.1029/2019GL086382.
- Gräler, B., Pebesma, E., and Heuvelink, G. Spatio-Temporal Interpolation using gstat. *The R Journal*, 8:204–218, 2016.
- Grendas, I., Theodoulidis, N., Hollender, F., and Hatzidimitriou, P. Spectral decomposition of S-waves in investigating regional dependent attenuation and improving site amplification factors: A case study in western Greece. *Bulletin of Earth-quake Engineering*, 20(12):1573–1456, 2022. doi: https://doi.org/10.1007/s10518-022-01459-z.
- Keilis-Borok, V. On estimation of the displacement in an earth-quake source and of source dimensions. *Ann. Geophys*, 12(2): 205–214, 1959. doi: doi.org/10.4401/ag-5718.
- Koenker, R. and Ng, P. SparseM: Sparse Linear Algebra. *R package version 1.81*, 2021.
- Koulakov, I., Bindi, D., Parolai, S., Grosser, H., and Milkereit, C. Distribution of Seismic Velocities and Attenuation in the Crust beneath the North Anatolian Fault (Turkey) from Local Earthquake Tomography. *Bulletin of the Seismological Society of America*, 100(1):207–224, 02 2010. doi: 10.1785/0120090105.
- Lavrentiadis, G., Abrahamson, N., and Kuehn, N. A non-ergodic effective amplitude ground-motion model for California. *Bullettin of Earthquake Engineering*, pages 5233–5264, 2023. doi: 0.1007/s10518-021-01206-w.
- Massicotte, P. and South, A. *rnaturalearth: World Map Data from Natural Earth*, 2023. R package version 1.0.1.
- Mayeda, K., Bindi, D., Roman-Nieves, J., Morasca, P., Dreger, D., Ji, C., Taira, T., Archuleta, R., Walter, W. R., and Barno, J. Source-Scaling Comparison and Validation for Ridgecrest, California: Radiated Energy, Apparent Stress, and Mw Using the Coda Calibration Tool (2.6<Mw<7.1). Bulletin of the Seismological Society of America, 11 2024. doi: 10.1785/0120240143.
- Meng, X. and Goulet, C. Lessons learned from applying varying coefficient model to controlled simulation datasets. *Bullettin of Earthquake Engineering*, pages 5151–5174, 2023. doi: 10.1007/s10518-022-01512-x.
- Molkenthin, C., Scherbaum, F., Griewank, A., Kuehn, N., and Stafford, P. A Study of the Sensitivity of Response Spectral Amplitudes on Seismological Parameters Using Algorithmic Differentiation. *Bulletin of the Seismological Society of America*, 104 (5):2240–2252, 08 2014. doi: 10.1785/0120140022.
- Mori, J., Abercrombie, R. E., and Kanamori, H. Stress drops and radiated energies of aftershocks of the 1994 Northridge, California, earthquake. *Journal of Geophysical Research: Solid Earth*, 108(B11), 2003. doi: https://doi.org/10.1029/2001JB000474.
- Nie, S. and Wang, Y. Revealing Spatial Variations of Earthquake Stress Drop and Peak Ground Acceleration Using

- a Non-Ergodic Modeling Framework. *Geophysical Research Letters*, 52(5):e2024GL112043, 2025. doi: https://doi.org/10.1029/2024GL112043.
- Oth, A., Bindi, D., Parolai, S., and Di Giacomo, D. Spectral Analysis of K-NET and KiK-net Data in Japan, Part II: On Attenuation Characteristics, Source Spectra, and Site Response of Borehole and Surface Stations. *Bulletin of the Seismological Society of America*, 101(2):667–687, 2011. doi: 10.1785/0120100135.
- Pebesma, E. Simple Features for R: Standardized Support for Spatial Vector Data. *The R Journal*, 10(1):439–446, 2018. doi: 10.32614/RJ-2018-009.
- Pebesma, E. J. and Bivand, R. Classes and methods for spatial data in R. *R News*, 5(2):9–13, 2005.
- R Core Team. R: A Language and Environment for Statistical Computing. R Foundation for Statistical Computing, Vienna, Austria, 2024
- Rekoske, J. M., Thompson, E. M., Moschetti, M. P., Hearne, M. G., Aagaard, B. T., and Parker, G. A. The 2019 Ridgecrest, California, Earthquake Sequence Ground Motions: Processed Records and Derived Intensity Metrics. *Seismological Research Letters*, 91(4): 2010–2023, 2020. doi: 10.1785/0220190292.
- Ross, Z. E., Idini, B., Jia, Z., Stephenson, O. L., Zhong, M., Wang, X., Zhan, Z., Simons, M., Fielding, E. J., Yun, S.-H., Hauksson, E., Moore, A. W., Liu, Z., and Jung, J. Hierarchical interlocked orthogonal faulting in the 2019 Ridgecrest earthquake sequence. *Science*, 366(6463):346–351, 2019. doi: 10.1126/science.aaz0109.
- Scherbaum, F. Combined inversion for the three-dimensional Q structure and source parameters using microearthquake spectra. *Journal of Geophysical Research: Solid Earth*, 95(B8):12423–12438, 1990. doi: https://doi.org/10.1029/JB095iB08p12423.
- Shearer, P. M., Vandevert, I., Fan, W., Abercrombie, R. E., Bindi, D., Calderoni, G., Chen, X., Ellsworth, W., Harrington, R., Huang, Y., Knudson, T., Roßbach, M., Satriano, C., Supino, M., Trugman, D. T., Yang, H., and Zhang, J. Earthquake Source Spectra Estimates Vary Widely for Two Ridgecrest Aftershocks Because of Differences in Attenuation Corrections. *Bulletin of the Seismological Society of America*, 12 2024. doi: 10.1785/0120240134.
- Shelly, D. R. A High-Resolution Seismic Catalog for the Initial 2019 Ridgecrest Earthquake Sequence: Foreshocks, Aftershocks, and Faulting Complexity. *Seismological Research Letters*, 91(4): 1971–1978, 01 2020. doi: 10.1785/0220190309.
- Shible, H., Hollender, F., Bindi, D., Traversa, P., Oth, A., Edwards, B., Klin, P., Kawase, H., Grendas, I., Castro, R. R., Theodoulidis, N., and Gueguen, P. GITEC: A Generalized Inversion Technique Benchmark. *Bulletin of the Seismological Society of America*, 112 (2):850–877, 02 2022. doi: 10.1785/0120210242.
- Stellato, B., Banjac, G., Goulart, P., Bemporad, A., and Boyd, S. OSQP: an operator splitting solver for quadratic programs. *Mathematical Programming Computation*, 12(4):637–672, 2020. doi: 10.1007/s12532-020-00179-2.
- Trugman, D. T. Stress-Drop and Source Scaling of the 2019 Ridge-crest, California, Earthquake Sequence. *Bulletin of the Seismological Society of America*, 110(4):1859–1871, 2020. doi: 10.1785/0120200009.
- University of Nevada, Reno. Nevada Seismic Network [Data set]., 1971
- University of Nevada, Reno. Southern Great Basin Network [Data set]., 1992.
- Vandevert, I. C., Shearer, P. M., and Fan, W. Ridgecrest Aftershock Stress Drops from P- and S-Wave Spectral Decomposition. *Bulletin of the Seismological Society of America*, 11 2024.

- doi: 10.1785/0120240133.
- White, M. C. A., Fang, H., Catchings, R. D., Goldman, M. R., Steidl, J. H., and Ben-Zion, Y. Detailed traveltime tomography and seismic catalogue around the 2019 Mw7.1 Ridgecrest, California, earthquake using dense rapid-response seismic data. *Geophysical Journal International*, 227(1):204–227, 06 2021. doi: 10.1093/gji/ggab224.
- Wickham, H. *ggplot2: Elegant Graphics for Data Analysis*. Springer-Verlag New York, 2016.
- Wickham, H., François, R., Henry, L., and Müller, K. *dplyr: A Grammar of Data Manipulation*, 2022. R package version 1.0.8.
- Wilke, C. O. cowplot: Streamlined Plot Theme and Plot Annotations for 'gaplot2', 2020. R package version 1.1.1.
- Zhang, J., Chen, X., and Abercrombie, R. E. Spatiotemporal Variability of Earthquake Source Parameters at Parkfield, California, and Their Relationship With the 2004 M6 Earthquake. *Journal of Geophysical Research: Solid Earth*, 127(6):e2021JB022851, 2022. doi: https://doi.org/10.1029/2021JB022851.

The article *Impact of Seismic Attenuation Corrections on Source Parameter Estimation* © 2025 by Dino Bindi is licensed under CC BY 4.0.